ACCOUNTS
of chemical research

Nanotubes from Chalcogenide Misfit Compounds: Sn—S and Nb—Pb—S

GAL RADOVSKY,[†] RONIT POPOVITZ-BIRO,[‡] DANIEL G. STROPPA,[§] LOTHAR HOUBEN,[§] AND RESHEF TENNE*,[†]

[†]*Department of Materials and Interfaces, Weizmann Institute, Rehovot 76100, Israel,* [‡]*Chemical Research Support Department, Weizmann Institute, Rehovot 76100, Israel, and* [§]*Peter Grünberg Institute and Ernst Ruska-Centre for Microscopy and Spectroscopy with Electrons, Forschungszentrum Jülich GmbH, 52425 Jülich, Germany*

RECEIVED ON MAY 19, 2013

CONSPECTUS

Carbon fullerenes and nanotubes revolutionized understanding of the reactivity of nanoscale compounds. Subsequently, our group and others discovered analogous inorganic compounds with hollow, closed nanostructures. Such inorganic nanostructures offer many applications, particularly in the energy and electronics industries.

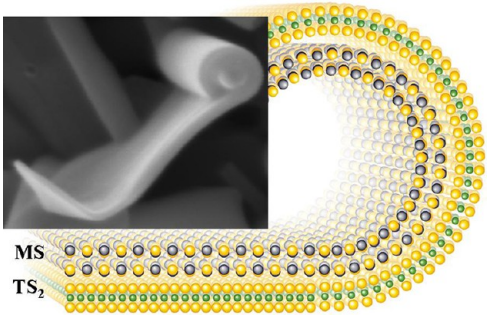

One way to create inorganic nanostructures is via misfit layered compounds (MLC), which are stacks of alternating two-dimensional molecular slabs, typically held together via weak van der Waals forces. They contain "misfits" in their *a*—*b* plane structures that can make them unstable, leading to collapse of the slabs into tubular nanostructures. For example, metal chalcogenide MLCs of the general formula $(MX)_{1+y}/TX_2$ (M = Sn, Pb, Bi, Sb, and other rare earths; T = Sn, Ti, V, Cr, Nb, Ta, etc.; X = S or Se) consist of a superstructure of alternating layers where the MX unit belongs to a (distorted NaCl) orthorhombic symmetry group (O), the TX_2 layer possesses trigonal (T) or octahedral symmetry, and the two layers are held together via both van der Waals and polar forces. A misfit in the *a* axis or both *a* and *b* axes of the two sublattices may lead to the formation of nanostructures as the lattices relax via scrolling. Previous research has also shown that the abundance of atoms with dangling bonds in the rims makes nanoparticles of compounds with layered structure unstable in the planar form, and they tend to fold into hollow closed structures such as nanotubes.

This Account shows that combining these two triggers, misfits and dangling bond annihilation in the slab rims, leads to new kinds of nanotubes from MLCs. In particular, we report the structure of two new types of nanotubes from misfits, namely, the SnS/SnS_2 and PbS/NbS_2 series. To decipher the complex structures of these nanotubes, we use a range of methods: high-resolution transmission electron microscopy (HRTEM), energy-dispersive X-ray spectroscopy (EDS), selected area electron diffraction (SAED) analyses, scanning electron microscopy (SEM), and Cs-corrected scanning transmission electron microscopy (STEM) in the high-angle annular dark-field mode (HAADF). In both new types, the lattice mismatch between the two alternating sublayers dictates the relative layer-stacking order and leads to a variety of chiral tubular structures. In particular, the incommensuration (a type of misfit) of the SnS_2/SnS system in both the (in plane) *a* and *b* directions leads to a variety of relative in-plane orientation and stacking orders along the common *c*-axis. Thus the SnS/SnS_2 nanotubes form superstructures with the sequence O—T and O—T—T, and mixtures thereof. We also report nanotubes of the misfit layered compound $(PbS)_{1.14}NbS_2$, and of NbS_2 intercalated with Pb atoms, with the chemical formula $PbNbS_2$. Thus, the possibility to use two kinds of folding mechanisms jointly offers a new apparatus for the synthesis of unique 1-D nanostructures of great complexity and a potentially large diversity of physicochemical properties.

Introduction

A new twist in the understanding of chemical reactivity in the nanoscale came with the discovery of carbon fullerenes[1] and nanotubes.[2] Equally important was the finding of hollow closed nanostructures of WS_2 first[3] and subsequently MoS_2[4] and BN.[5] Thus, the concept of hollow, closed nanostructures transcended into the realm of the vast field of inorganic compounds with layered structure.

Published on the Web 09/17/2013 www.pubs.acs.org/accounts
10.1021/ar400138h

These compounds are made of 2-D molecular slabs stacked together via weak van der Waals forces. It was proposed that the loosely bonded rim atoms would lead to inherent instability of the planar MoS_2 nanosheets, where the ratio of rim to bulk atoms is very large, provoking folding of the layer into hollow cage structures, that is, multiwall quasi-spherical (fullerene-like) nanostructures (IF) and nanotubes (INT). Obviously, these multiwall nanotubes are stable in the nanoscale only.[6] Being globally less stable than the macroscopic sheet, they can be obtained via kinetically controlled reactions only. Contrarily, a variety of naturally occurring alumo (magnesium)-silica minerals, like immogolite,[7] chrysotile,[8] and hallyosite,[9] which have asymmetric structure along the stacking (*c*) axis, are thermodynamically stable in the nanotubular form as manifested through their existence over geological time scales and theoretical works.[10,11] The first classification between these two families of layered compounds and the folding tendency of the asymmetric ones was established by Pauling.[12]

Another family of materials with asymmetric structure are the misfit layered compounds (MLC), which are made of alternating stacking of molecular layers with different chemical composition and periodicities. They usually form an incommensurate or a semi-incommensurate lattice, at least along one direction. These compounds have been investigated quite intensively for several decades.[13−16] In particular, the series of MLCs $(MX)_{1+y}(TX_2)_m$ (M = Sn, Pb, Bi, Sb, or rare earths; T = Sn, Ti, V, Cr, Nb, or Ta; X = S or Se; $0.08 < y < 0.32$; $m = 1-3$) was investigated thoroughly.[14−16] The *c*-axis is the stacking direction, and the incommensuration is expressed as $a_{MX} \neq a_{TX_2}$ (generally, the *b*-axis is almost identical for the two compounds). MX is an orthorhombic bilayer (consisting of two distorted 002-oriented planes) aligned periodically perpendicular to the common "*c*"-axis, while TX_2 crystallizes in a trigonal-prismatic or octahedral (pseudohexagonal) lattice as roughly shown in Figure 1a.

Also generally, $y = 4/2(a_{TX_2}/a_{MX}) - 1$, where the ratio $4/2 = 2$ is determined by the number of formula units in the unit cell of each sublattice (4 for MX and 2 for TX_2). The parameter "*m*" is an integer representing the number of TX_2 units alternating with the MX unit in the superstructure ($m = 1$, 2, or 3) in a single $(MX)_{1+y}(TX_2)_m$ molecular slab (along the *c*-axis). The interaction between the two subsystems leads to modulation of the lattice structure, which was studied by electron diffraction.[17] Therefore, the $(MX)_{1+y}(TX_2)_m$ system forms a global supersymmetry, which may be different, in general, from the lattice symmetry of each of the comprising bulk crystals.

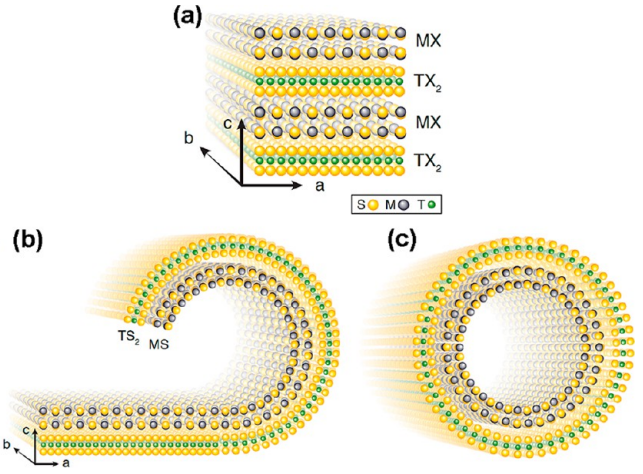

FIGURE 1. Schematic representation of (a) the structure of the $(MX)_{1+y}(TX_2)$ misfit compound, (b) the structure of the $(MS)_{1+y}(TS_2)$ misfit compound at initiation of the bending, and (c) formation of the tubular structure.

Recent advances in materials synthesis provide a new tool to fabricate new $[(MSe)_{1+y}]_n(TSe_2)_m$ superstructures with T = W, Mo, or Ta and M = Pb or Sn with much larger control and versatility than before.[19,20]

Much knowledge on the relaxation mechanisms of the lattice strain in MLC was known before from detailed XRD analysis[14−16] and electron diffraction data.[17,18] The formation of cylindrical MLC from $MX-TX_2$ was discussed in some detail, mostly in connection with the mineral cylindrite.[13,18] More recently this relaxation mechanism was discussed in the context of tubes and scrolls produced from the MLCs $(PbS)_{1.14}(NbS_2)_2$[21] and $(BiS)_{1.17}(NbS_2)_n$[22] with $n = 1-4$. As a first approximation, the radius of curvature is determined by the mismatch between the *a*-axes of the two sublattices.[21] Additionally, the relatively large thickness of the molecular slab, ~1.2−3 nm, and the high rigidity of the bonds was thought to impose a steric hindrance on the radius of curvature of the "misfit" layers.

Indeed, MLCs are suitable candidates to form rolled-up structures in the form of tubes or scrolls. An example for such structures is the "misfit" tube with the stoichiometry $(PbS)_{1.14}(NbS_2)_2$.[21] The tubule axis is expected to coincide with the commensurate *b* direction. Surprisingly, most $PbS_{1.14}(NbS_2)_2$ tubes were found to be chiral.[21] This fact was attributed to the small misfit between the *b* axes of the pristine compounds, which accommodates elastically and causes the axis of curvature to deviate somewhat from the "commensurate" direction, that is, lead to chiral tubes.[21] Spontaneous bending is mostly expected for an asymmetric lamella, that is, limited on one side by a MS and on the other side by a TS_2 layer as shown in Figure 1.

This driving force is complementary to the already established closure mechanism, that is, annihilation of the dangling bonds at the periphery of the layers of the inorganic nanotube (INT) nanostructures.[3]

Recognizing the fact that the driving force for the scrolling of misfit structures is disparate from the stimulus to form carbon nanotubes or those of WS_2 and MoS_2, it is quite natural to hypothesize that the two independent stimuli can be combined and activated simultaneously, leading to a new kind of nanotubular structures from MLCs. With that notion in mind, a new strategy to synthesize nanotubes from the misfit compound SnS–SnS_2, which is the first example of this new series, was uncovered. Obviously, other mechanisms, like the well-known vapor–liquid–solid (VLS) method, can be also engendered for the growth of nanotubes from 2-D compounds.[23] Furthermore, the "misfit" driving force was discussed in terms of the difference in lattice constants at room temperature[21] and is likely to differ for the relevant growth temperatures.

SnS–SnS_2 Nanotubes

In the SnS–SnS_2 system, the relevant bulk structures forming the MLC possess a layered structure. α-SnS_2 crystallizes in the CdI_2 layered structure[24–26] with a pseudohexagonal unit cell sometimes referred as trigonal (T). The simplest polytype of SnS_2 with a space group $P\bar{3}m1$ is designated either 1T or 2H depending on the system of labeling with $a = 0.36486$ nm and $c = 0.58992$ nm and one sulfur–metal–sulfur triple layer as a repeat unit. α-SnS (*Pnma*), the bulk phase Herzenbergite, has a GeS structure with an orthorhombic (O) (highly distorted NaCl) unit cell. The lattice parameters of this phase are $a = 1.118$ nm, $b = 0.398$ nm, and $c = 0.432$ nm.[27] (Note that in order to be consistent with different literature sources and avoid confusion, the usually referred *c*-axis of SnS, which is perpendicular to the basal planes, is represented by the index "*h*" in the *hkl* notation). In both compounds, the layers are stacked together by weak van der Waals forces and some degree of polar bond formation (partial charge transfer).

Figure 2 shows a hedgehog-like agglomerate of SnS–SnS_2 superstructure tubular nanocrystals with different internal structures obtained via high temperature vapor transport of Sn–S species in the presence of bismuth and antimony sulfide catalysts.[28,29] The interplanar spacings of both SnS_2 and SnS layers measured from the selected area electron diffraction (SAED) patterns of Sn–S tubules are unchanged relative to the bulk counterparts within 3%.[29] Therefore, unlike in the SnS–NbS_2[30] and PbS–NbS_2 systems,[21] it is believed that in the SnS–SnS_2 "misfit" system, both SnS_2 and

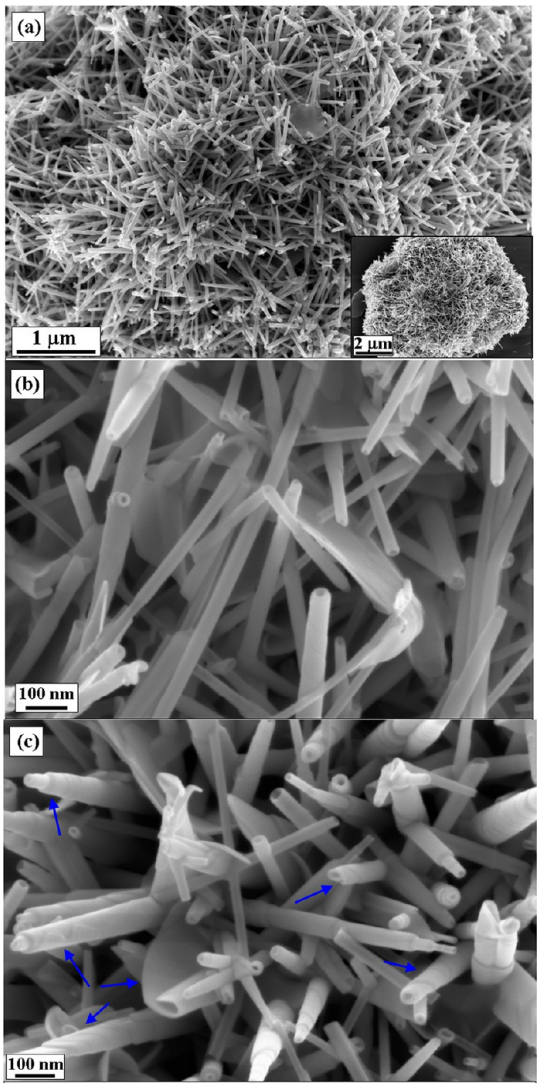

FIGURE 2. Low (a) and high (b, c) magnification scanning electron microscopy (SEM) images of a "hedgehog-like" agglomerate of SnS–SnS_2 tubules with different internal structure and morphology. The hollow cores, the scrolling process, and the scrolling steps are clearly visible in panel b and marked by blue arrows in panel c.

SnS almost retain their original bulk structure upon stacking. Consequently, misfit occurs along the two in-plane directions (*a* and *b*). Another example for such two-axis mismatch is shown for the $(PbSe)_{0.99}WSe_2$, (PbSe)$MoSe_2$, and (SnSe)$MoSe_2$ systems.[19] Such two axis mismatch may lead to different in-plane orientations between the SnS and SnS_2 layers and different folding vectors. Also, the diversity of different internal structures of the tubules is a result of different periodicities along the common "*c*"-axis between the SnS_2 and SnS layers with stoichiometries of $(SnS)_{1.32}(SnS_2)$, $(SnS)_{1.32}(SnS_2)_2$, and $[(SnS)_{1.32}]_2(SnS_2)_3$, designated as O–T, O–T–T, and O–T–O–T–T, respectively.[29] A superstructure sheet in the scrolling process and tubules with apparent scrolling steps are marked

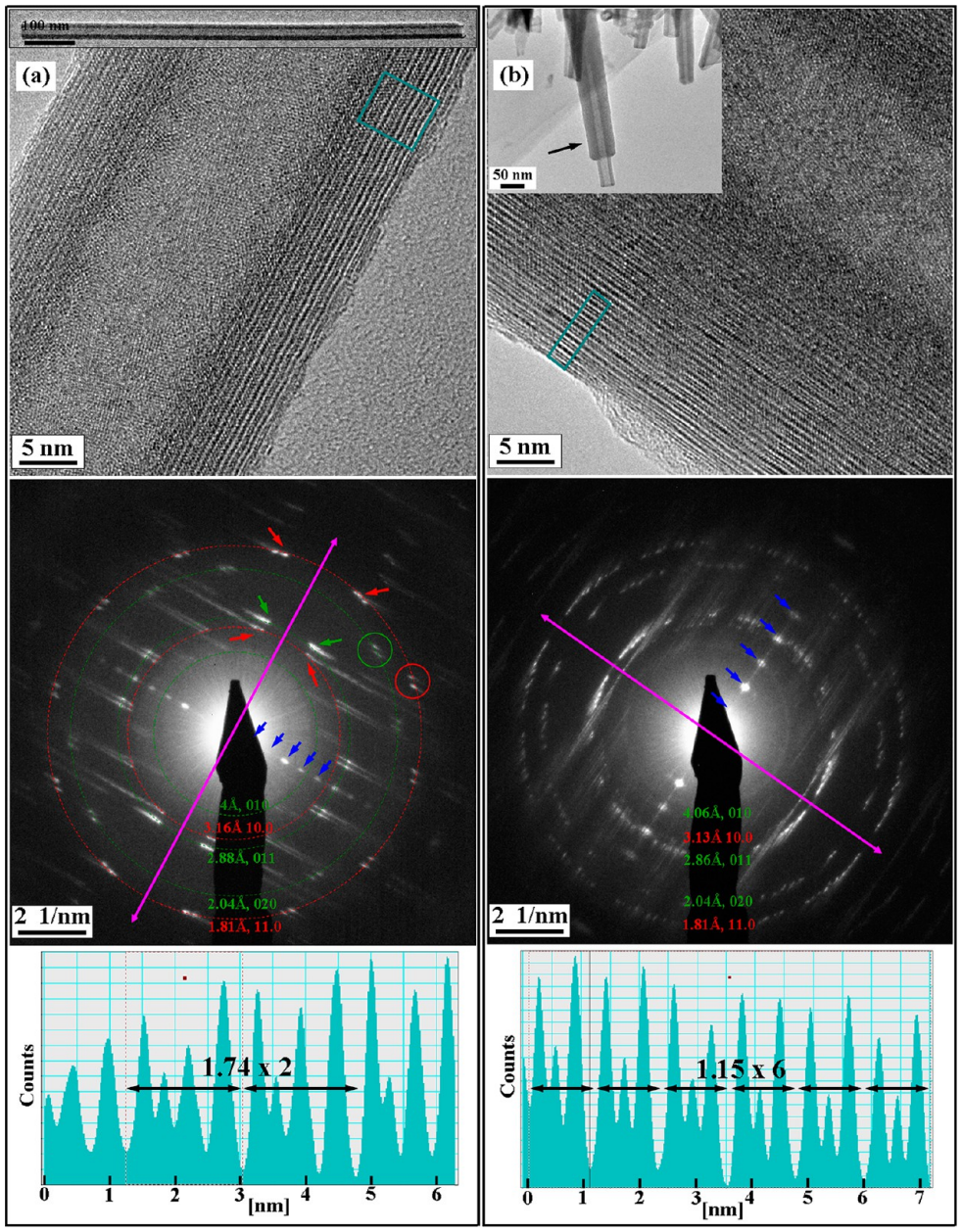

FIGURE 3. (a) TEM images of SnS/SnS_2 tubule with O−T−T periodicity. (top) High and low (inset) magnification images. (middle) SAED pattern taken from the area shown in the high-magnification image. Tubule axis is marked by a pink double arrow. Spots pertinent to the same interplanar spacing are marked by segmented circles and their measured values and Miller indices are indicated. Red circles correspond to SnS_2 and green to SnS. Blue arrows mark the basal reflections produced by the superstructure. (bottom) Line profile obtained from the region enclosed in the rectangle in the upper image. (b) TEM images of $SnS-SnS_2$ tubule with O−T periodicity. (top) High and low (inset) magnification images. (middle) SAED pattern taken from the area shown in the high-magnification image. Notation is similar to panel a. (bottom) Line profile obtained from the region enclosed in the rectangle in the upper image.

by blue arrows in Figure 2c. The existence of dislocation-like defects (not shown here) suggests that the transition from the scroll-like to the concentric tubes occurred mainly by dislocation mechanism as was shown also for graphite.[31] However, no direct online evidence for the "zippering" of edges, which is a key step for the transition from a nanoscroll into nanotube, was observed so-far.

Figure 3a shows a TEM image of the most commonly encountered SnS/SnS_2 nanotube with O−T−T superstructure having 1.74 nm periodicity. The periodicity is clearly seen in the line profile and can also be deduced from the series of basal reflections in the diffraction pattern as marked by the blue arrows in the diffraction pattern (first and second order are covered under the central beam). The

reflections of SnS_2 pertinent to (10.0) and (11.0) planes (in hexagonal systems *hk.l* is equivalent to the notation *hkil* with $i = -(h + k)$) are marked by red segmented circles while the 010 and 011 reflections of SnS are marked by the green segmented circles. The interplanar spacings are indicated in the diffraction pattern. They are all in good agreement with values of bulk SnS_2[25,26] and SnS[27] single crystals within 3% deviation. Such a deviation can be attributed to strain-induced variation of the interplanar distances but also to the limited precision of the distance measurements between the corresponding spots.

In the current tube, there are 12 sets of 10.0 and 11.0 reflections of SnS_2, which are distributed with equal azimuthal angle from each other on the red segmented circles of the SAED pattern. The multiplicity factors (the number of equivalent planes) for both these planes are six. Also, two couples of the 11.0 and the 10.0 diffraction spots of the SnS_2 (marked by short red arrows; out of the total 12 pairs for each (11.0) and (10.0) planes) almost coincide with the tubule axis (pink double arrow). Such an observation suggests the occurrence of two different rolling vectors of the SnS_2 layers within the same tubule. For SnS, two of its 011 couples of spots (out of the eight pairs) almost coincide with the tubule axis (marked by green arrows). Therefore, the axis of the tube almost coincides with the normal to (011) planes of SnS. Furthermore, the 011 spots of SnS azimuthally coincide with the 10.0 spots of SnS_2 (see for example green and red arrows). Therefore, the in-plane orientation between the SnS_2 and SnS layers can be determined, see Figure 5d in ref 29. This configuration is relevant to most of the nanotubes observed in this study. However, in a few percent of the tubules, the normal to the (010) planes of SnS coincides with the normal to the (10.0) planes of SnS_2 and with the tube axis as was previously shown.[28]

The helical arrangement of the SnS_2 and SnS layers manifests itself through the difference in the orientation of the atomic lattice on the top and the bottom walls of the tubule. Each of the top and bottom walls of a helical tube with a single helix angle will give rise to splitting of the 11.0, 10.0, 010, and 011 spots of SnS_2 and SnS, respectively. The chiral angle can be estimated from the splitting of the mentioned reflections in the diffraction pattern and equals half the angle of the azimuthal splitting of the spots.

The chiral angle of the SnS_2 layers was determined from the azimuthal splitting of the 11.0 sets as marked by red small circle in the diffraction pattern and was found to be $\sim$1.4°. For SnS, a value of $\sim$1.5° was determined from the splitting of the four sets of the 010 reflections or more clearly from their second-order 020 spots as marked by the green small circle in the diffraction pattern in Figure 3a.

Figure 3b shows an example of the second most commonly encountered SnS−SnS_2 nanotube with O−T superstructure and 1.15 nm periodicity. The periodicity is shown in the line profile and confirmed also by the series of basal reflections in the diffraction pattern as marked by the blue arrows (first order is covered under the central beam). In that specific tubule, the 10.0, 11.0, 010, and 011 reflections of SnS_2 and SnS form almost a ring-like pattern indicating the presence of multiple helicities. Alternately, such a pattern can be obtained from a scroll-like nanostructure. A more detailed analysis of these nanostructures was presented previously.[29] The tubule has a telescopic structure and is a part of big hedgehog-like tubular agglomerate (similar to that shown in Figure 2).

Nb−Pb−S Nanotubes

Among the different phases existing in the Nb−S system,[32] the relevant bulk structures for MLCs are the layered structures of NbS_2. Several polytypes exist for bulk NbS_2, which differ in the stacking of the layers along the *c*-axis. In the bulk pseudohexagonal phase ($P6_3/mmc$), the Nb atoms are located in octahedral or trigonal prismatic sites between two hexagonally close packed sulfur layers forming a three-atom layered sandwich structure. The in-plane lattice parameter is $a = 0.331$ nm, and *c* is an integer multiple of 0.5945 nm, depending on the stacking order. However, in the tubular structures reported here, two adjacent layers of NbS_2 along the *c*-axis were not observed. Bulk PbS ($Fm\bar{3}m$) exhibits a rock-salt structure with a lattice parameter of 0.5934 nm.[33] However, upon stacking with NbS_2 layers the structure is modified as will be discussed later.

Figure 4 shows Nb−Pb−S superstructure tubular nanocrystals with different internal structures. Two main kinds of nanotubes were observed here: first, tubules with a periodicity of 1.19 nm along the common *c*-axis with theoretical stoichiometry of $(PbS)_{1.14}NbS_2$; second, $PbNbS_2$ tubules with a periodicity of 0.88 nm along the *c*-axis, which can be visualized as staging $n = 1$ Pb-intercalated NbS_2 nanotubes. For the former, single in-plane orientation between the NbS_2 and PbS layers and two different folding vectors for the superstructure layer were observed. Both the $(PbS)_{1.14}NbS_2$ and $PbNbS_2$ groups contain cylindrical and conical tubular nanocrystals as shown also in Figure 5 and Figure S1 of the Supporting Information.

$(PbS)_{1.14}NbS_2$ Tubules with 1.19 nm Periodicity along the *c*-Axis

Figure 5 shows details of the TEM analyses of two kinds of PbS−NbS_2 nanotubes, which differ in their folding vector.

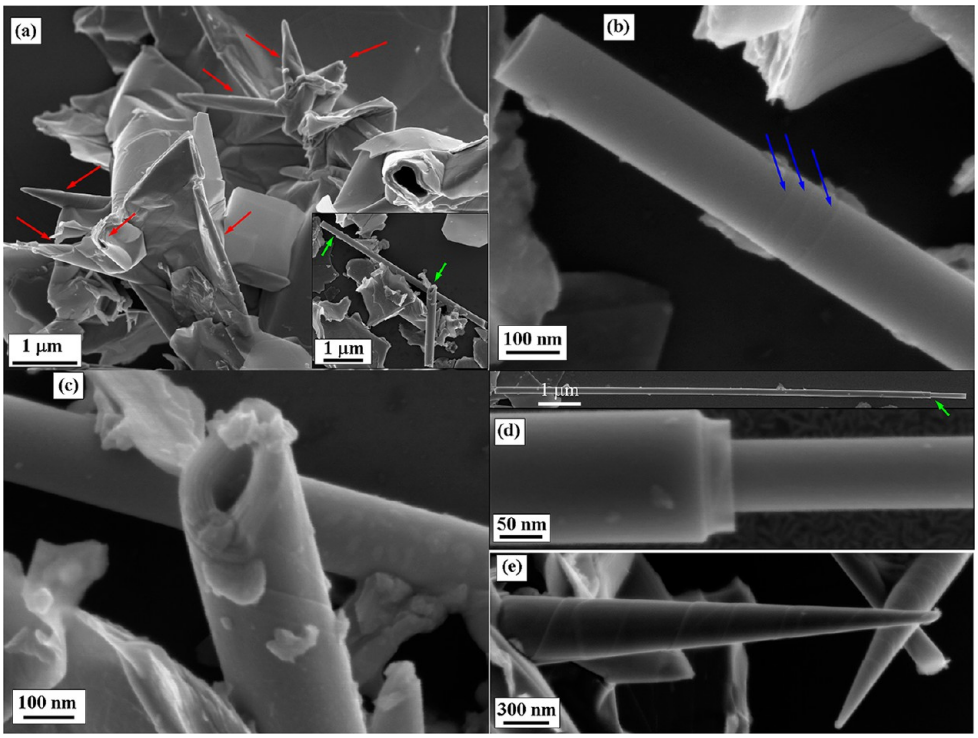

FIGURE 4. (a) SEM image of a Nb−Pb−S slab being partially scrolled into tubular crystals, which are marked by red arrows. (b, c) High magnification images of the tubules in panel a marked by green arrows. Growing steps are marked by blue arrows. (d) Low and high magnification images of a straight long tubule with telescopic step. High magnification image taken from the area marked by a green arrow. (e) Conical tubules with apparent scrolling steps.

Figure 5a shows an example of $(PbS)_{1.14}NbS_2$ tubule with 1.19 nm periodicity as shown in the line profile in Figure 5c. The tubules consist of alternating layers of NbS_2 and PbS. The periodicity along the *c*-axis can also be confirmed by the basal reflections marked by blue arrows in the diffraction pattern in Figure 5b and also clearly visible in the Cs-corrected scanning transmission electron microscopy (STEM)−high-angle annular dark-field mode (HAADF) image in Figure 5d. The interplanar spacings and the Miller indices are indicated on the diffraction pattern. The diffraction pattern in Figure 5b clearly shows 12 sets of reflections that are equally azimuthally distributed on a circle (as marked by the big red segmented circles) with interplanar spacings of 1.67 and 2.88 Å. Such distances match the interplanar spacings of (11.0) and (10.0) planes of NbS_2, respectively[32] (ICSD col. code 43697). The multiplicity factors for these planes are six (which is half of the produced reflections). A couple (out of the 12) of both the 11.0 and 10.0 diffraction spots coincide with the tubule axis and are marked by orange arrows. This suggests that, in analogy to the Sn−S case, two different rolling vectors of the NbS_2 layers occur within the same tubule. In addition, all 12 sets of spots are splintered by similar angle, and two of them are marked by red double arrows as shown in the diffraction pattern in Figure 5b. Such a splitting arises from the chiral folding of the layers and the chiral angle of 5.5°, which equals half of the azimuthal splitting of the spots, 11° in this case.

The spots with measured interplanar spacings of 4.08 Å and its second order 2.04 Å are attributed to PbS layers. The noted interplanar spacings match the spacings of the (110) and (220) planes of the layered PbS with space group $Cm2a$[34] (ICSD col. code 68701). This PbS polytype is known to occur in MLCs and is different from bulk PbS. The multiplicity factor for these planes is four. However, the diffraction pattern clearly shows 12 pairs of equa-azimuthally splintered couples of spots. As often occurs in MLCs, the MX layer is being modified to adapt to the hexagonal TX_2 layer, and one of its lattice parameters accommodates a lattice parameter of $\sim(\sqrt{3})a$ of the TX_2 layer, say NbS_2 in this case. Therefore it is convenient to define the pseudohexagonal TX_2 with ortho-hexagonal unit cell with a, $b=(\sqrt{3})a$, and c as lattice parameters as shown in Figure 6a. In this tube, the *b* direction of PbS is parallel to the *b* direction of the ortho-hexagonal NbS_2, and both these lattice parameters are almost equal. Therefore, the 010 and 020 spots of PbS are expected to coincide with the tubule axis as well as the 10.0

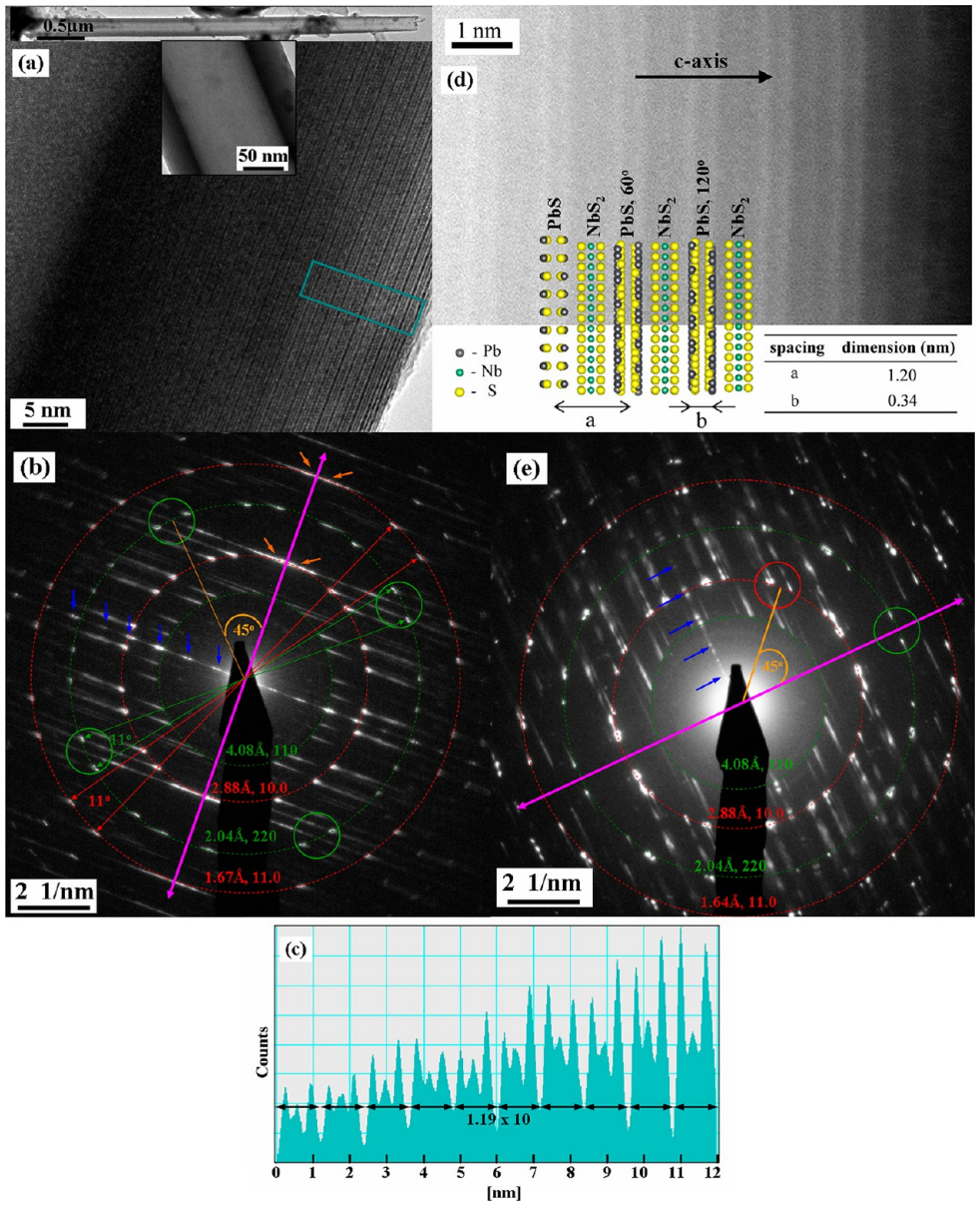

FIGURE 5. TEM images of $(PbS)_{1.14}NbS_2$ tubules with 1.19 nm periodicity. (a) High, medium, and low (insets) magnification images. (b) SAED pattern taken from the area shown in panel a. Tubule axis is marked by a pink double arrow. Spots pertinent to the same interplanar spacing are marked by segmented rings and their measured values and pertinent Miller indices are indicated (for NbS_2, hexagonal labeling system is used). Red circles correspond to NbS_2 and green to PbS. Red and green double arrows point to the spots of NbS_2 and PbS used for the determination of the chiral angles. Blue arrows indicate a basal reflection produced from a superstructure. See text for small green circles and short orange arrows. (c) Line profile integrated along the region enclosed in the rectangle in panel a. (d) STEM−HAADF image of another $(PbS)_{1.14}NbS_2$ nanotube similar in structure to that shown in panel a and atomistic model of the tubule in the inset. (e) SAED pattern of another $(PbS)_{1.14}NbS_2$ tubule with 1.19 nm periodicity exhibiting different folding vector than that shown in panel b. The notation is the same as that in panel b. See text for red and green small circles.

of NbS_2, see the diffraction pattern in Figure 5b. (The (10.0) plane of NbS_2 according to the pseudohexagonal notation is equivalent to the (020) of the ortho-hexagonal notation). However no diffraction spots pertinent to the (010) or (020) planes of PbS were observed, probably due to the missing reflections in the PbS lattice. Instead, four couples of 110 spots (marked by green circles) appear at 45° azimuth from the tubule axis as shown in Figure 5b, that is, in agreement with the calculated angle of 44.8° between (010) and (110) planes (the multiplicity factor for the {110} planes of PbS is four). Since there are three equivalent *"b"* directions in NbS_2 that are rotated by 60° as marked by the green arrows in Figure 6a, there are two additional layers of PbS (three in-total), all of which are rotated by 60° relative to each other about the common *c*-axis. Consequently, there are three quartets of 110 spots of PbS azimuthally rotated by 60° from

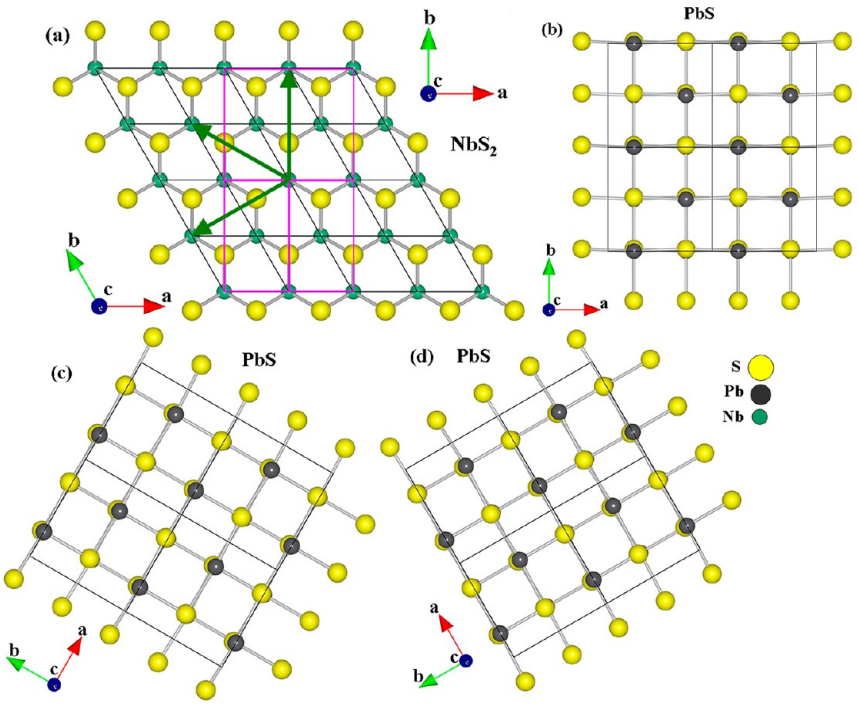

FIGURE 6. (a) Schematic model of single layer of NbS_2 annotated according to the pseudohexagonal and ortho-hexagonal coordinates, black and purple unit cells, respectively. Three equivalent "*b*" directions are indicated by green arrows according to the ortho-hexagonal unit system. Panels b, c, and d are single PbS layers: panel c is rotated by 60° and panel d by 120° relative to panel b in such a way that their *b*-axes are parallel to one of the equivalent *b*-axis of NbS_2, which marked by green arrows in panel a.

each other, virtually forming 12 pairs of equi-azimuthally splintered couples of spots as clearly seen in Figure 5b.

Due to the 6-fold symmetry of {10.0} planes of NbS_2, these two additional PbS layers form equivalent orientation with respect to the adjacent NbS_2. However, their folding vector is different and their *b*-axis deviates from the tubule's axis.

Also, as in the case of NbS_2, 12 couples of PbS spots are azimuthally splintered within a chiral angle of $11°/2 = 5.5°$ as marked by the green double arrows.

In many cases two couples of the 110 (or 220) spots (and not the 010) of PbS coincide with the tubule axis as marked by the small green circle in the diffraction pattern in Figure 5e. Consistently with the previous example, the 10.0 spots of NbS_2 (or 020 according to the ortho-hexagonal system of labeling, the *b*-axis), which are expected to be parallel to the 020 of PbS, azimuthally deviate from the tubule axis by ~45° as marked by small red circle in the diffraction pattern in Figure 5e. Such an observation is indicative of a similar in-plane orientation between the NbS_2 and PbS layers; however the folding vector is different from the case shown in Figure 5b. This observation suggests that the tubule axis does not coincide with the *b*-axis of the two sublattices in this case.

$PbNbS_2$ Tubules with 0.88 nm Periodicity along the *c*-Axis

Figure 7 shows an example of a $PbNbS_2$ tubule with 0.88 nm periodicity along the *c*-axis as shown in the line profile and confirmed by appropriate basal reflections in the diffraction pattern marked by blue arrows. It is believed that such a structure is analogous to the one reported in the ICSD col. code 74698 with $P6_3/mmc$ space group.[35] The transition metal (Nb) is in trigonal-prismatic coordination with respect to the chalcogen (S) atoms, while the Pb atoms are intercalated inside the van der Waals gap between each two adjacent NbS_2 layers (staging $n = 1$) and form a linear coordination with the sulfur layers of NbS_2 as shown in the model in Figure 7d. This structure could be stabilized through partial charge transfer driven coordination. Figure 7d shows a STEM−HAADF image of another $PbNbS_2$ nanotube with similar structure to the one shown in panel a. Since HAADF is sensitive to Z-contrast, layers of NbS_2 appear dark, while monolayers of Pb appear bright.

The interplanar spacings of 1.7 and 2.96 Å in Figure 7c are in agreement with the inteplanar spacings of 1.67 and 2.9 Å of the (10.0) and (11.0) planes of Pb-intercalated NbS_2, respectively (see ICSD col. code 74698). These two planes exhibit six sets of spots (marked by red arrows), which is in

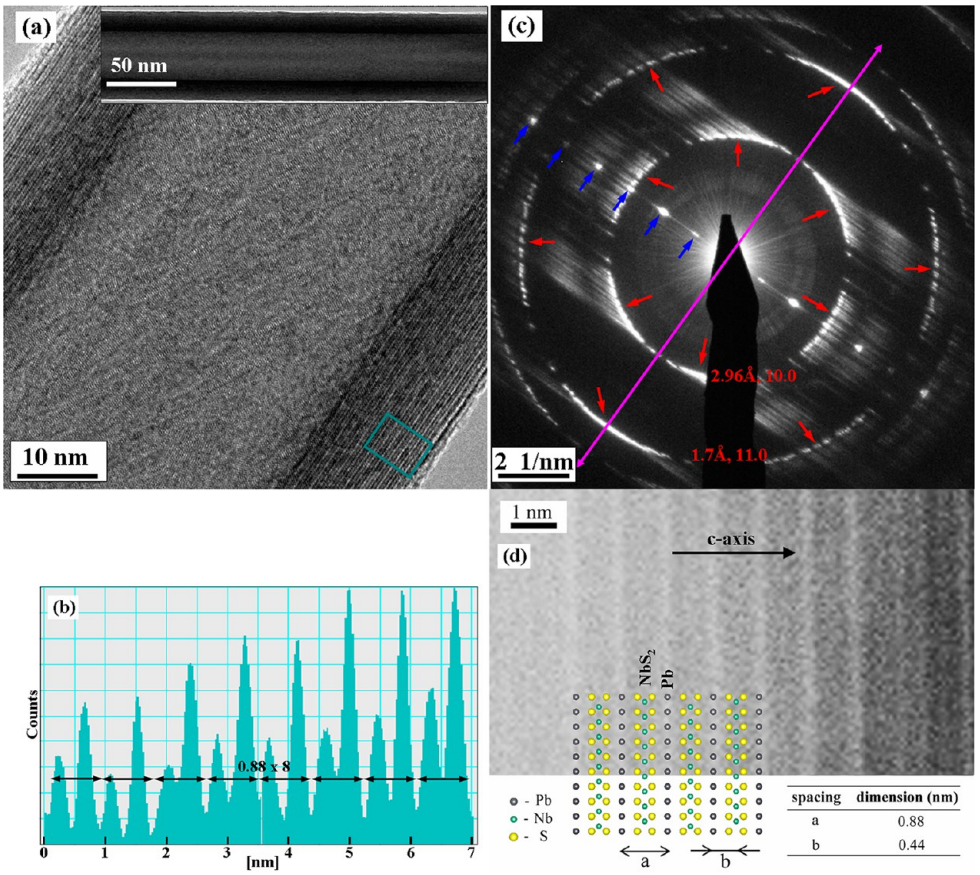

FIGURE 7. (a) High and low (inset) magnification TEM images of $PbNbS_2$ tubule with 0.88 nm periodicity. (b) Line profile integrated along the region enclosed in the rectangle in panel a. (c) SAED pattern taken from the area shown in panel a. Tubule axis is marked by a pink double arrow. Measured interplanar spacings and their pertinent Miller indices are indicated on ring-like patterns (for NbS_2 hexagonal labeling system is used). Six short red arrows point to a sets of spots indicating 6-fold symmetry of the structure. (d) STEM–HAADF image of another $PbNbS_2$ nanotube similar in structure to that shown in panel a, with the atomistic model of the nanotube.

agreement with the multiplicity factor of 6 for both of them.[35]

Chemical analysis of the $(PbS)_{1.14}NbS_2$ and the $PbNbS_2$ nanotubes (shown in Figure S2 in the Supporting Information) yields an atomic ratio close to 1:1 between the niobium and lead atoms, which is in agreement with the theoretical stoichiometry. However, since the L lines of Pb and K lines of Nb are used for the calculations, their accuracy is compromised. Another factor hindering the precision of these calculations is the known overlap between the Pb M_α, Nb L_β, and S K_α lines.

The use of energy-dispersive X-ray spectroscopy (EDS) here is supportive and is not expected to be fully quantitative. However, electron diffraction and HAADF can be actually used for absolute verification of the stacking order and assigning the accurate structures of the misfit nanotubes (work in progress). In the SnS/SnS_2 and $(PbS)_{1.14}NbS_2$, the formation of the concentric nanotubes initiates, most likely, with a formation of a scroll. On the other hand, the $PbNbS_2$ nanotubes, which are sometime more than 10 μm long and have uniform inner and outer diameters (see Figure S3 in the Supporting Information) are believed to grow unidirectionally. This growth mode can be promoted by liquid lead. In fact one such long nanotube filled with lead in its core was analyzed by STEM–EDS as shown in the Supporting Information in Figure S3. Lead filling occurs also for conical tubes as well as cylindrical ones as shown in Figure S1b of the Supporting Information. Also, the presence of tubules with mixed periodicities (as shown in Figure S4 in the Supporting Information) suggests a combination of possible growth mechanisms.

On the average, Nb–Pb–S tubules exhibit bigger outer and inner diameters compared with their Sn–S counterparts. The typical outer diameters of Sn–S nanotubes range between 20 and 60 nm while those of Nb–Pb–S are between 50 and 250 nm. Outer diameters of up to 500 nm were observed for the Nb–Pb–S tubules compared with 160 nm for the Sn–S ones. The larger diameter of the Nb–Pb–S nanotubes may arise from the higher rigidity of the chemical bonds which manifests itself through higher folding energies.

In conclusion, this work shows that the driving force for the growth of nanotubular geometry in this family of compounds is the misfit between different constituent layers combined with the chemical energy savings due to the healing of the dangling bonds at the periphery of the layers.

Experimental Section

Synthesis of Sn−S Nanotubes. For the synthesis of the Sn−S tubular nanostructures, SnS_2, SnS, Bi, and Sb_2S_3 powders were inserted into a quartz ampule at a molar ratio of ∼6:2:2:1, sealed in vacuum, and inserted into a vertical 1-zone reactor furnace. The high-temperature annealing procedure involved two steps. First, the ampule was kept at a temperature gradient of ∼790 °C at the bottom (with the precursors) and ∼110 °C at the upper edge for 1 h. Next, the ampule was moved inside the furnace and subjected to an opposite temperature gradient of ∼790 °C at the upper edge and ∼150 °C at the bottom for 50 min. The product accumulated at the bottom cold edge of the ampule.

Synthesis of Nb−Pb−S Nanotubes. For the synthesis of the Nb−Pb−S tubular structures, Nb, PbS, sulfur (molar ratio of ∼2.5:1:1.5), and minuscule amounts of $PbCl_2$ were inserted into a quartz ampule and sealed in vacuum. The performed high-temperature annealing procedure involved two steps. The first step involved heating at a temperature gradient with 350 °C (bottom with the precursors) and ∼850 °C (upper edge) for 1 h. Next, the ampule was moved inside the furnace and subjected to an opposite temperature gradient, i.e. ∼850 °C (bottom edge with the precursors) and ∼400 °C at the upper edge for 8 h. The product accumulated at the upper cold edge of the ampule.

Electron Microscopy. For TEM, the suspension with the product was dripped on carbon/colloidion-coated lacey Cu grids. Si/Al SEM stubs were prepared in a similar fashion. The resulting samples were examined by Philips CM120 TEM, operating at 120 kV and FEI Technai F20 operating at 200 kV, equipped with HAADF detector for STEM. Both microscopes were equipped with EDS detector (EDAX-Phoenix Microanalyzer). Many of the analyses were performed with FEI Technai F30-UT high-resolution transmission electron microscopy (HRTEM) operating at 300 kV. Zeiss Ultra model V55 SEM and FEI Titan-S Cs-corrected STEM operating at 300 kV were also utilized. High-angle annular dark field (HAADF) signal was acquired within a 78−440 mrad angular range.

Conclusions

Nanotubes of the misfit SnS/SnS_2 compound with different superstructure orders were prepared. In most nanotubes, the normal to the (10.0) planes of SnS_2 was found to be almost parallel to the normal to the (011) planes of SnS determining thereby the in-plane orientation. However, several exceptions were encountered, suggesting different in-plane orientations such as when the normal to (010) planes of SnS is parallel to the normal to (10.0) planes of SnS_2.[28]

In the $PbS−NbS_2$ system, the PbS and NbS_2 layers are commensurate along the *b* direction (when considering orthohexagonal system for NbS_2) and the fact that the *b* axis of NbS_2 is parallel to the *b*-axis of PbS determines their in-plane orientation. However, two main folding vectors were observed: first, when the tubule axis coincides with the common *b*-axis and leads the incommensurate *a*-directions of the layers to be the folding directions; second, when the normal to the (110) plane of PbS coincides with the nanotube axis. For both the $PbS−NbS_2$ and Sn−S systems, it is believed that concentric tubule formation is promoted by the initial rolling of the $MS−TS_2$ superstructure sheets and nanoscroll formation (see Figure S5 in the Supporting Information). $PbNbS_2$ tubules with 0.88 nm periodicity consist of intercalated Pb atoms in linear coordination between the sulfur atoms of the two adjacent NbS_2 layers. The high length and uniform outer and inner diameters suggest that one-dimensional growth occurs for such nanotubes.

Supporting Information. Conical tubules, chemical analysis, tubules filled with lead, tubules with a stacking disorder, and $(PbS)_{1.14}NbS_2$ tubules with partly rolled superstructure sheet. This material is available free of charge via the Internet at http://pubs.acs.org.

R.T. gratefully acknowledges the support of ERC (Project INTIF 226639), the Israel Science Foundation, Harold Perlman Foundation, and the GMJ Schmidt Minerva Center. He is the Drake Family Chair in Nanotechnology and director of the Helen and Martin Kimmel Center for Nanoscale Science. The Irving and Cherna Moskowitz Center for Nano and Bio-Nano Imaging is also acknowledged.

BIOGRAPHICAL INFORMATION

Gal Radovsky received his B.Sc. (2007) and M.Sc. (2009) degrees in Materials Engineering from the Ben-Gurion University (Israel). He is currently a Ph.D. student at the Weizmann Institute of Science under the supervision of Prof. Reshef Tenne.

Ronit Popovitz-Biro finished her Ph.D. (Weizmann Institute of Science) in 1980 and did her postdoctoral research at the University of California, San Diego (1982−1984). Since 1998, she is a senior staff scientist at the Weizmann Institute of Science.

Daniel G. Stroppa received his B.Sc. degree in Engineering Physics from Federal University of São Carlos (Brazil) in 2007 and

Ph.D. degree in Mechanical Engineering from State University of Campinas (Brazil) in 2011. He currently works as a postdoctoral researcher at Forschungszentrum Jülich (Germany).

L. Houben received his Ph.D. degree in physics in 1998 from the Heinrich-Heine-Universität Düsseldorf. He is a research staff member in the Ernst Ruska-Centre for Microscopy and Spectroscopy with Electrons at the Forschungszentrum Jülich.

Prof. Reshef Tenne is a member of the Israeli Academy of Sciences and Academia Europaea. He is credited with the discovery of the inorganic nanotubes and fullerene-like nanoparticles from layered compounds.

FOOTNOTES

*Corresponding author. Phone: +972-8-934-2394. Fax: +972-8-934-4138. E-mail: reshef.tenne@weizmann.ac.il.

The authors declare no competing financial interest.

REFERENCES

1 Kroto, H. W.; Heath, J. R.; O'Brien, S. C.; Curl, R. F.; Smalley, R. E. C_{60}: Buckminsterfullerene. *Nature* **1985**, *318*, 162–163.

2 Iijima, S. Helical Microtubules of Graphitic Carbon. *Nature* **1991**, *354*, 56–58.

3 Tenne, R.; Margulis, L.; Genut, M.; Hodes, G. Polyhedral and Cyllindrical Structures of Tungsten Disulphide. *Nature* **1992**, *360*, 444–446.

4 Feldman, Y.; Wasserman, E.; Srolovitz, D. J.; Tenne, R. High Rate, Gas Phase Growth of MoS_2 Nested Inorganic Fullerenes and Nanotubes. *Science* **1995**, *267*, 222–225.

5 Chopra, N. G.; Luyken, R. J.; Cherrey, K.; Crespi, V. H.; Cohen, M. L.; Louie, S. G.; Zettl, A. Boron Nitride Nanotubes. *Science* **1995**, *269*, 966–967.

6 Seifert, G.; Köhller, T.; Tenne, R. Stability of Metal Chalcogenide Nanotubes. *J. Phys. Chem. B* **2002**, *106*, 2497–2501.

7 Mukherjee, S.; Kim, K.; Nair, S. Short, Highly Ordered, Single-Walled Mixed-Oxide Nanotubes Assemble from Amorphous Nanoparticles. *J. Am. Chem. Soc.* **2007**, *129*, 6820–6826.

8 Falini, G.; Foresti, E.; Gazzano, M.; Gualtieri, A. F.; Leoni, M.; Lesci, I. G.; Roveri, N. Tubular-Shaped Stoichiometric Chrysotile Nanocrystals. *Chem.—Eur. J.* **2004**, *10*, 3043–3049.

9 Abdullayev, E.; Sakakibara, K.; Okamoto, K.; Wei, W.; Ariga, K.; Lvov, Y. Natural Tubule Clay Template Synthesis of Silver Nanorods for Antibacterial Composite Coating. *ACS Appl. Mater. Interfaces* **2011**, *3*, 4040–4046.

10 Konduri, S.; Mukherjee, S.; Nair, S. Strain Energy Minimum and Vibrational Properties of Single-Walled Aluminosilicate Nanotubes. *Phys. Rev. B* **2006**, *74*, No. 033401.

11 Zhao, M.; Xia, Y.; Mei, L. Energetic Minimum Structures of Imogolite Nanotubes: A First-Principles Prediction. *J. Phys. Chem. C* **2009**, *113*, 14834–14837.

12 Pauling, L. The Structure of the Chlorites. *Proc. Natl. Acad. Sci. U. S. A.* **1930**, *16*, 578–582.

13 Makovicky, E.; Hyde, B. G. Non-Commensurate (Misft) Layer Structures. *Struct. Bonding (Berlin)* **1981**, *48*, 101–l75.

14 Meerschuat, A. Misfit Layer Compounds. *Curr. Opin. Solid State Mater. Sci.* **1996**, *1*, 250–260.

15 Rouxel, J.; Meerscheut, A. Misfit Layer Compounds $(MX)_n(TX_2)_m$. *Mol. Cryst. Liq. Cryst. Sci. Technol., Sect. A* **1994**, *244*, 343–354.

16 Wiegers, G. A.; Meerschaut, A. Misfit Layer Compounds $(MS)_nTS_2$. Structure and Physical Properties. *Mater. Sci. Forum* **1992**, *100—101*, l01–l72.

17 Kuypers, S.; Van Landuyt, J. Electron Microscopy of Incommensurate Intergrowth Structures "MTS_3. *Mater. Sci. Forum* **1992**, *100—101*, 223–272.

18 Williams, T. B.; Hyde, B. G. Electron Microscopy of Cylindrite and Franckeite. *Phys. Chem. Miner.* **1988**, *15*, 521–544.

19 Smeller, M. M.; Heideman, C. L.; Lin, Q.; Beekman, M.; Anderson, M. D.; Zschack, P.; Anderson, I. M.; Johnson, D. C. Structure of Turbostratically Disordered Misfit Layer Compounds $[(PbSe)_{0.99}]_1[WSe_2]_1$, $[(PbSe)_{1.00}]_1[MoSe_2]_1$, and $[(SnSe)_{1.03}]_1[MoSe_2]_1$. *Z. Anorg. Allg. Chem.* **2012**, *638*, 2632–2639.

20 Lin, Q.; Smeller, M.; Heideman, C. L.; Zschack, P.; Koyano, M.; Anderson, M. D.; Kykyneshi, R.; Keszler, D. A.; Anderson, I. M.; Johnson, D. C. Rational Synthesis Characterization of a New Family of Low Thermal Consuctivity Misfit Layer Compounds $[(PbSe)_{0.99}]_m(WSe_2)_n$. *Chem. Mater.* **2010**, *22*, 1002–1009.

21 Bernaerts, D.; Amelinckx, S.; Van Tendeloo, G.; Van Landuyt, J. Microstructure and Formation Mechanism of Cylindrical and Conical Scrolls of the Misfit Layer Compounds $PbNb_nS_{2n+l}$. *J. Cryst. Growth* **1997**, *172*, 433–439.

22 Gomez-Herrero, A.; Landa-Canovas, A. R.; Otero-Diaz, L. C. Electron Microscopy Study of tubular crystals $(BiS)_{1+\delta}(NbS_2)_n$. *Micron* **2000**, *31*, 587–595.

23 Yella, A.; Mugnaioli, E.; Panthofer, M.; Therese, H. A.; Kolb, U.; Tremel, W. Bismuth-Catalyzed Growth of SnS_2 Nanotubes and Their Stability. *Angew. Chem., Int. Ed.* **2009**, *48*, 6426–6430.

24 Sharma, R. C.; Chang, Y. A. The S-Sn (Sulfur-Tin) System. *Bull. Alloy Phase Diagrams* **1986**, *7*, 269–273.

25 Mitchell, R. S. Structural Polytypism of SnS_2. *Nature* **1974**, *247*, 537–538.

26 Al-Alami, F. A. S.; Balchin, A. A.; White, M. The Expansivities and the Thermal Degradation of Some Layer Compounds. *J. Mater. Sci.* **1977**, *12*, 2037–2042.

27 del Buccia, S.; Jumas, J. C.; Maurin, M. Contribution a l'Etude de Composes Sulfures d'Etain(II): Affinement de la Structure de SnS. *Acta Crystallogr.* **1981**, *B37*, 1903–1905.

28 Radovsky, G.; Popovitz-Biro, R.; Staiger, M.; Gartsman, K.; Thomsen, C.; Lorenz, T.; Seifert, G.; Tenne, R. Synthesis of Copious Amounts of SnS_2 and SnS_2/SnS Nanotubes with Ordered Superstructures. *Angew. Chem., Int. Ed.* **2011**, *50*, 12316–12320.

29 Radovsky, G.; Popovitz-Biro, R.; Tenne, R. Study of Tubular Structures of the Misfit Layered Compound SnS_2/SnS. *Chem. Mater.* **2012**, *24*, 3004–3015.

30 Wiegers, G. A.; Meerschaut, A. J. Structures of Misfit Layer Compounds $(MS)_nTS_2$ (M=Sn, Pb,Bi, Rare Earth Metals; T=Nb,Ta,Ti,V,Cr; 1.08<n<1.23). *J. Alloys Compd.* **1992**, *178*, 351–368.

31 Pokropivny, A. V.; Pokropivny, V. V. Dislocation Mechanism of Nanotube Formation. *Tech. Phys. Lett.* **2003**, *29*, 494–495.

32 Jellinek, F.; Brauer, G.; Mueller, H. Molybdenum and Niobium Sulphides. *Nature* **1960**, *185*, 376–377.

33 Noda, Y. Charge Distribution and Atomic Thermal Vibration in Lead Chalcogenide Crystals. *Acta Crystallogr.* **1983**, *B39*, 312–317.

34 Wiegers, G. A.; Meetsma, A.; Haange, R. J.; van Smaalen, S.; de Boer, J. L. The Incommensurate Misfit Layer Structure of $(PbS)_{l.14}NbS_2$, `$PbNbS_3$' and $(LaS)_{1.14}NbS_2$, `LaNbS3': An X-ray Diffraction Study. *Acta Crystallogr.* **1990**, *B46*, 324–332.

35 Eppinga, R.; Wiegers, G. A. A Generalized Scheme for Niobium and Tantalum Dichalcogenides Intercalated with Post-Transition Elements. *Physica* **1980**, *99B*, 121–127.